



**HAL**  
open science

# Micellar-Mediated Block Copolymer Ordering Dynamics Revealed by In Situ Grazing Incidence Small-Angle X-Ray Scattering during Spin Coating

Guillaume Fleury, Daniel Hermida-Merino, Dong Jingjin, Karim Aissou, Aleksei Bytchkov, Giuseppe Portale

► **To cite this version:**

Guillaume Fleury, Daniel Hermida-Merino, Dong Jingjin, Karim Aissou, Aleksei Bytchkov, et al.. Micellar-Mediated Block Copolymer Ordering Dynamics Revealed by In Situ Grazing Incidence Small-Angle X-Ray Scattering during Spin Coating. *Advanced Functional Materials*, 2019, 29 (10), pp.1806741. 10.1002/adfm.201806741 . hal-02323201

**HAL Id: hal-02323201**

**<https://hal.science/hal-02323201v1>**

Submitted on 30 May 2022

**HAL** is a multi-disciplinary open access archive for the deposit and dissemination of scientific research documents, whether they are published or not. The documents may come from teaching and research institutions in France or abroad, or from public or private research centers.

L'archive ouverte pluridisciplinaire **HAL**, est destinée au dépôt et à la diffusion de documents scientifiques de niveau recherche, publiés ou non, émanant des établissements d'enseignement et de recherche français ou étrangers, des laboratoires publics ou privés.



Distributed under a Creative Commons Attribution 4.0 International License

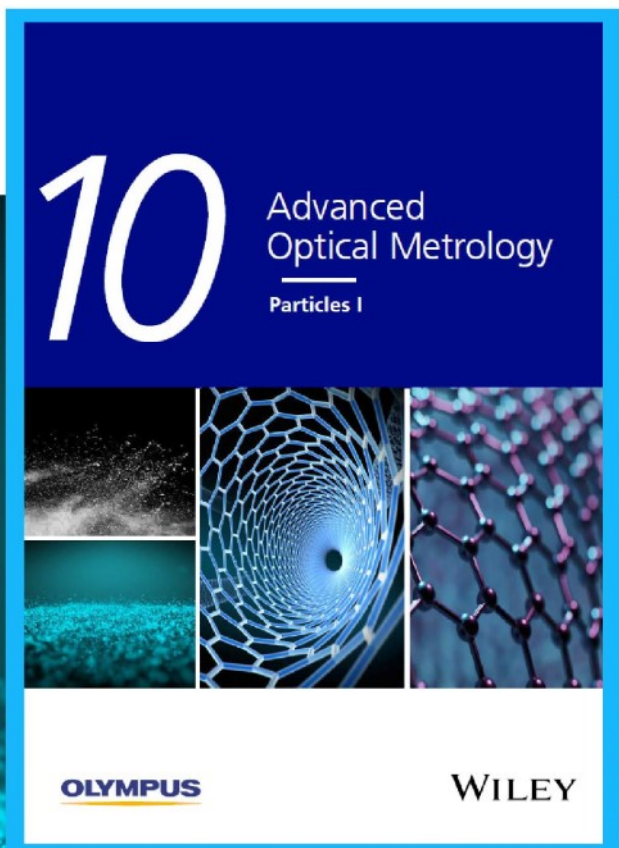


# Particles I

Access the latest eBook →

Particles: Unique Properties,  
Uncountable Applications

**Read the latest eBook and  
better your knowledge with  
highlights from the recent  
studies on the design and  
characterization of micro-  
and nanoparticles for  
different application areas.**



**Access Now**

This eBook is sponsored by

**OLYMPUS**

**WILEY**

# Micellar-Mediated Block Copolymer Ordering Dynamics Revealed by In Situ Grazing Incidence Small-Angle X-Ray Scattering during Spin Coating

Guillaume Fleury,\* Daniel Hermida-Merino, Dong Jingjin, Karim Aissou, Aleksei Bytchkov, and Giuseppe Portale\*

Spin coating is one of the most versatile methods to generate nanostructured block copolymer (BCP) thin films which are highly desired for many applications such as nanolithography or organic electronics. The self-assembly pathways through phase separation, both in solvent and in bulk, strongly influence the final BCP structure obtained after spin coating. As a demonstration, the formation of highly ordered in-plane lamellae is elucidated herein by using in situ grazing incidence small-angle X-ray scattering. A key step in this complex fast organization process is the formation of intermediate micellar phases triggered by solvent affinity toward one of the block. Indeed, directional coalescence of a short-lived intermediate hexagonal structure of cylindrical micelles enables the development of a final highly ordered lamellar structure, predominantly oriented parallel to the substrate surface. These results suggest that the existence of such transient micellar phases is a crucial process in order to produce highly ordered structures with a specific orientation directly after the BCP thin film deposition; and should be the focus of further optimization for the directed self-assembly and, more generally, in the bottom-up nanostructure fabrication.

nanostructured membranes,<sup>[8–10]</sup> sensors,<sup>[11]</sup> photonics,<sup>[12–14]</sup> and solar cells.<sup>[15,16]</sup> In all the aforementioned fields, the BCP ordering pathways can be tailored to achieve a multitude of nanostructures with the desirable orientation and periodicity. Several methods are commonly used to process BCP thin films including dip coating,<sup>[17]</sup> drop casting,<sup>[18,19]</sup> and zone casting.<sup>[20]</sup> Among the different methods, spin coating is considered as the most versatile methodology to produce uniform sub-micrometer BCP layers with a precise control of the film characteristics through the deposition parameters. At the end of the spin coating process, the resulting BCP nanostructure is often kinetically trapped, far from the equilibrium structure, since solvent selectivity, evaporation rate, substrate topography, and interfacial interactions apply strong constraints on the thermodynamic phase separation

process.<sup>[21–25]</sup> Therefore, an additional annealing treatment of the polymeric layers (mainly through thermal or solvent vapor annealing) is often mandatory to enhance the BCP chain mobility, leading to an improved long-range ordering of the nanostructure.<sup>[26,27]</sup>

In situ grazing incidence small-angle X-ray scattering (GISAXS) has emerged as a powerful tool for characterizing the structural development of the BCP morphological features as it can reveal both the self-organization mechanism and the kinetics during the annealing steps. As recently reviewed by Müller-Buschbaum,<sup>[28]</sup> it allows accessing the 3D morphology and understanding the 3D defects in BCP thin films. In situ GISAXS has been thoroughly used in the past to investigate the transient BCP structures and the transformation pathways occurring between the different states during thermal<sup>[29–31]</sup> or solvent vapor<sup>[32]</sup> annealing. Inherently more challenging due to the short timescale of the process is the in situ observation of the BCP structural development and the detection of possible transient states during spin coating. Such information is of primordial importance to further control the final BCP morphology and orientation, as a variety of nonequilibrium BCP morphologies can be obtained by adjusting the spin coating process parameters (i.e., solvent selectivity, evaporation rate, film thickness).<sup>[23,33–35]</sup> While visible light scattering<sup>[36]</sup> and even stroboscopic optical microscopy<sup>[37,38]</sup> techniques have been successfully used in the past to observe phase separation during spin coating process, the BCP phase separation behavior at

Periodic structures of nanometer length scale formed by ordered block copolymer (BCP) thin films constitute a versatile platform<sup>[1–3]</sup> to provide significant development in many technological applications such as data storage,<sup>[4,5]</sup> lithography,<sup>[6,7]</sup>

Dr. G. Fleury, Dr. K. Aissou

Laboratoire de Chimie des Polymères Organiques (LCPO)  
CNRS UMR 5629–ENSCP–Université de Bordeaux  
16 Avenue Pey-Berland F-33607, Pessac Cedex, France  
E-mail: gfleury@enscp.fr

Dr. D. Hermida-Merino, Dr. A. Bytchkov

DUBBLE CRG BM26@ESRF  
Netherlands Organization for Scientific Research (NWO)  
71 Avenue des Martyrs 38000, Grenoble, France

D. Jingjin, Dr. G. Portale

Macromolecular Chemistry & New Polymeric Materials  
Zernike Institute for Advanced Materials  
University of Groningen  
Nijenborgh 4 9747, AG, The Netherlands  
E-mail: g.portale@rug.nl

 The ORCID identification number(s) for the author(s) of this article can be found under <https://doi.org/10.1002/adfm.201806741>.

© 2019 The Authors. Published by WILEY-VCH Verlag GmbH & Co. KGaA, Weinheim. This is an open access article under the terms of the Creative Commons Attribution License, which permits use, distribution and reproduction in any medium, provided the original work is properly cited.

The copyright line for this article was changed on 1 April 2020 after original online publication.

DOI: 10.1002/adfm.201806741

the characteristic 10–100 nm length scale cannot be studied by these techniques. Conversely, these characteristic dimensions are perfectly suited for GISAXS. Moreover, with the advent of synchrotron GISAXS and the use of state of the art noiseless 2D detectors,<sup>[39,40]</sup> in situ experiments are becoming more feasible and successful examples have been recently reported mostly for polymer blends.<sup>[41–46]</sup> To the best of our knowledge, only a few studies reported in situ GISAXS measurements of BCP ordering during spin coating.<sup>[41,47,48]</sup>

In this work, in situ GISAXS measurements were performed to monitor the structural development of parallel lamellae formed by poly(1,1-dimethyl silacyclobutane)-*block*-poly(methyl methacrylate) (PDMSB-*b*-PMMA) thin films spin coated from a BCP solution in a mixture of two solvents, one common for the two blocks and one selective for only one block. Although the directed self-assembly of these PDMSB-*b*-PMMA chains into a thin film cylindrical structure has been demonstrated at equilibrium (i.e., through thermal annealing treatment),<sup>[49,50]</sup> the complex thermodynamic interactions between the different blocks and the solvent mixture, consisting of high and low boiling point solvents, yield to the formation of highly ordered in-plane lamellae after the spin coating process. Controlling and stabilizing with high reproducibility a certain morphology characterized by an excellent long-range order is of key importance for BCP nanotechnology and, through this study, we sought to better apprehend the mechanisms leading to segregated structures and acting during the spin coating process.

The PDMSB-*b*-PMMA system used in this study has a molecular weight of 14.3 kg mol<sup>-1</sup> and a PDMSB volume fraction,  $\phi_{\text{PDMSB}}$ , of 0.72.<sup>[49]</sup> The synchrotron SAXS powder pattern obtained on thermally annealed sample (see Figure S1A, |Supporting Information) was indexed with a *p6mm* symmetry of the cylindrical morphology with a lattice parameter,  $a_{\text{CYL}} = 2/\sqrt{3}D_{10}^{\text{CYL}} = 20.5$  nm. This result is in agreement with the structure and pitch observed on nanostructured thin film samples casted from a 2 wt% BCP solution (tetrahydrofuran/propylene glycol monomethyl ether acetate THF/PGMEA: 70/30) and annealed at 180 °C for 10 min, since in-plane PMMA cylinders ( $a_{\text{CYL}} = 20.8$  nm) are observed on the atomic force microscopy (AFM) phase view presented in Figure 1A. The corresponding GISAXS patterns (see Figure S1B,C, Supporting Information) support this morphological assignment, as the observed diffraction features are consistent with hexagonally structured domains aligned with their {10} planes parallel to the film surface. In contrast, the PDMSB-*b*-PMMA thin film directly after the spin coating process exhibits a featureless surface with the evidence of some sparse terraces (Figure 1B). The corresponding scanning transmission electron microscopy (STEM) image presented in the Figure 1C reveals that parallel lamellae with  $D_{10}^{\text{LAM}} \approx 13$  nm are formed within the PDMSB-*b*-PMMA thin film after deposition. The parallel orientation of the lamellar structure is also confirmed by the 2D GISAXS pattern presented in Figure 1D which mainly consists of intensity modulations, referred as diffuse Bragg sheets (DBSs),<sup>[51,52]</sup> along the

vertical  $q_z$  direction and strongly focused around  $q_y = 0$  nm<sup>-1</sup>. This behavior is indicative of a lamellar morphology oriented parallel with respect to the substrate plane.<sup>[51]</sup> The periodicity of the parallel lamellar structure can be also retrieved from the analysis of the GISAXS vertical intensity cuts extracted from Figure 1D using the distorted wave born approximation theory.<sup>[51,53]</sup> Due to fact that a rod-like-shaped beamstop was used in this study, the specular rod along  $q_y = 0$  nm<sup>-1</sup> is not accessible. Instead the vertical cuts have been computed right next to the beamstop along  $q_y = 0.05$  nm<sup>-1</sup>. Considering the nature of the scattering pattern of the in-plane lamellar morphology, these two vertical cuts are virtually equivalent. The lamellar spacing just after the spin coating was calculated using Equation (1),<sup>[32,51]</sup> taking into account the first two pairs of diffracted peaks (*minus*  $M_1$ ,  $M_2$  and *plus*  $P_1$ ,  $P_2$  branches) from the GISAXS profile presented in Figure S2 in the Supporting Information.

$$q_z = k_{i,z} + \sqrt{k_{c,\text{film}}^2 + \left[ \frac{2\pi m}{D_{10}^{\text{LAM}}} \pm \sqrt{k_{i,z}^2 - k_{c,\text{film}}^2} \right]^2} \quad (1)$$

where  $k_{i,z} = \frac{2\pi}{\lambda} \sin(\alpha_i)$  and  $k_{c,\text{film}} = \frac{2\pi}{\lambda} \sin(\alpha_{c,\text{film}})$  are the  $z$ -component of the wave vector of the incoming X-ray beam and the wave vector at the critical angle of total external reflection of the PDMSB-*b*-PMMA BCP including the absorbed PGMEA, respectively.  $m$  is the order of the reflection and  $D_{10}^{\text{LAM}}$  the parallel lamellar spacing.

The determination of the parallel lamellar spacing according to Equation (1) gives  $D_{10}^{\text{LAM}} = 16$  nm with a fitted incident angle of 0.115° and polymer critical angle of 0.09°, very close to the expected values. The discrepancy between the lamellar periodicity obtained from STEM and GISAXS analyses can be easily understood if we consider that STEM analysis is performed under high vacuum, leading to evaporation of the residual solvent contained in the PDMSB-*b*-PMMA thin film. The fraction of the solvent trapped within the lamellar phase,  $\phi_{\text{solv}}$ , can be estimated from the ratio of the interdomain spacing in the dry state,  $D_{\text{dry}}^{\text{LAM}}$ , and the wet state,  $D_{\text{wet}}^{\text{LAM}}$ ,  $\phi_{\text{solv}} = 1 - \frac{D_{\text{dry}}^{\text{LAM}}}{D_{\text{wet}}^{\text{LAM}}} \approx 0.19$ .

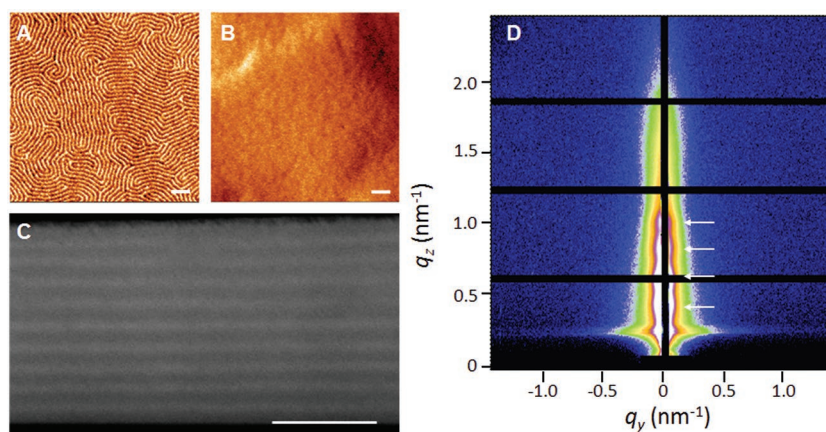


**Figure 1.** A) AFM phase view (scale: 100 nm) of the nanostructured BCP thin film after thermal annealing at 180 °C. B,C) AFM phase (scale: 100 nm) and STEM cross-sectional (scale: 50 nm) views of the nanostructured BCP thin film after spin coating. D) GISAXS pattern of the nanostructured BCP thin film after spin coating. The white arrows point to the observed diffuse Bragg sheets (DBSs).

Interestingly, this value is in good agreement with the macroscopic solvent fraction estimated using the film thickness,  $\phi_{\text{soil}} = 1 - \frac{h_{\text{dry}}^{\text{film}}}{h_{\text{wet}}^{\text{film}}} \approx 0.2$ . This observation, associated together with the strongly focused scattering intensity around the specular direction, suggests that nearly 100% of the lamellar grains have parallel orientation with respect to the substrate.<sup>[52]</sup> Moreover, the correlation length,  $\xi_{\text{LAM}}$ , (length scale over which the positional order of the lamellar structure is preserved) in the direction perpendicular to the substrate can be estimated as  $\xi_{\text{LAM}} = \frac{2\pi}{\Delta q_z} = 143$  nm, where  $\Delta q_z$  is the width of the  $M_1$  or  $P_1$  lamellar peaks in Figure S2 in the Supporting Information. This value is very close to the final thickness of 150 nm measured right after the spin coating via profilometry and white light reflectance, confirming the high degree of order of the parallel lamellar structure throughout the whole film.

As already mentioned above, the lamellar morphology is not expected at equilibrium since a cylindrical structure is produced from thermally annealed PDMSB-*b*-PMMA samples (see Figure 1A) in accordance with the BCP composition in the dry state ( $f_{\text{PDMSB}} = 0.72$ ) and previous data.<sup>[49]</sup> From the thermodynamic point of view, this discrepancy can be explained by considering the selective location of the high boiling PGMEA solvent inside the minor PMMA domains (PDMSB homopolymer chains show a low solubility in PGMEA), thus altering the phase diagram and shifting the structure from cylindrical to lamellar morphology. This is fully supported by the calculated BCP composition in the swollen state, considering that about 20% of solvent is sequestered within the PMMA domains after spin coating ( $f_{\text{PDMSB}} = 0.57$ ). Upon thermal annealing, the solvent is evaporated from the PMMA domains and the expected cylindrical structure is retrieved.

From these preliminary observations, the preferential sequestration of PGMEA within the PMMA domains allows to understand the formation of lamellae. However, the overall quality of the BCP structure, consisting of long-range ordered in-plane lamellae, is rather unexpected with respect to previously reported GISAXS experiments on BCP thin films after casting, in which poorly ordered structures were observed directly after spin coating.<sup>[29,53–57]</sup> Indeed, only few low energy dislocations sparsely distributed within the PDMSB-*b*-PMMA layers are observed from STEM images, making that the PDMSB and PMMA domains are separated by well-defined flat interfaces (see Figure 1C). These results are also supported by the 2D GISAXS pattern of the as-cast PDMSB-*b*-PMMA thin film which exhibits only straight and narrow DBS as opposed to diffuse Debye–Scherrer rings expected for randomly oriented lamellar grains. The formation of a non-equilibrium parallel lamellar structure with an extremely high order leads to open questions regarding the assembly pathways followed by PDMSB-*b*-PMMA chains during a wet deposition process and, more importantly, how the casting parameters could alter the resulting nanostructured BCP thin film (i.e., defectivity, domain orientation and long-range ordering). Moreover, preassembly in solution of the PDMSB-*b*-PMMA chains has to be considered since preformed micellar structures are commonly used as template to achieve BCP thin films with the desired nanostructure.<sup>[5,58–61]</sup> Control over the micellar structure formation, their packing and the coalescence process adds consequently further

leverage to tune thin film BCP structures resulting from wet deposition processes.

In order to elucidate the formation mechanism of this highly ordered parallel lamellar structure observed here, we have performed in situ GISAXS measurements during spin coating at 1000 rpm of a 2 wt% BCP solution in THF/PGMEA: 70/30. The GISAXS images (163 ms per frame) were acquired during solvent evaporation using an incident angle of 0.12° which is around the substrate critical angle and slightly above the polymer critical angle ( $\alpha_{\text{c,BCP}} = 0.1^\circ$ ). Laser interferometry was simultaneously used to measure the wet layer thickness during drying, thus allowing a simple method to monitor the solvent and solid fractions during spin coating (Figure 2A,B).<sup>[42]</sup> Typical 2D GISAXS patterns at selected times are shown in Figure 2C–E while the evolution of horizontal and vertical intensity cuts is reported in Figure 2F,G. For  $t \leq 2.1$  s, the rapid lateral ejection of the BCP solution in excess from the substrate takes place. Neither diffuse nor diffracted intensity is detected and the BCP solution is homogeneous. For spin coating time  $2.1 \text{ s} \leq t \leq 10.8$  s, THF evaporates first due to its lower boiling point and higher vapor pressure, and diffuse scattering, especially along the  $q_y$  direction, is visible (see Figure 2C,F). Such a diffuse scattering intensity is associated to the formation of BCP micelles in the drying wet layer. Unfortunately, the recorded intensity during the fast GISAXS acquisition is too weak to perform a detailed analysis of the micellar shape. However, since the BCP fraction as a function of time can be retrieved from the laser interferometry data ( $\phi_{\text{BCP}} = \frac{h_{\text{wet}}^{\text{film}}(t = \infty)}{h_{\text{wet}}^{\text{film}}(t = x)}$ ), we have performed solution SAXS analysis at approximately the same BCP concentration in PGMEA, even if caution should be exercised in the direct comparison between the equilibrated micellar structure probed by SAXS and the rapidly evolving micellar structure observed during the GISAXS experiments. Note that tetrahydrofuran (THF) has fully evaporated from the drying wet layer from  $t > 4$  s according to the abrupt change in slope of the thickness versus time curve obtained from the laser interferometry data. At  $t = 5$  s, the BCP fraction is about 0.05 and the solution SAXS profile collected at this polymer concentration in PGMEA resembles the GISAXS intensity during spin coating at 5 s (see Figure S3, Supporting Information). Best fit of the 5 wt% BCP solution SAXS intensity shows the presence of core–shell elliptical BCP micelles with minor, major semiaxes and shell thickness of  $a = 6.7$  nm,  $b = 60$  nm, and  $s = 3$  nm, respectively (see Figure S4, Supporting Information). Additional dynamic light scattering measurements (see Table S1, Supporting Information) confirm the presence of micellar objects with a hydrodynamic radius  $R_{\text{H}}^{\text{DLS}} = 30$  nm in close agreement with the solution SAXS results ( $R_{\text{H}}^{\text{SAXS}} = \sqrt[3]{(a+s)(b+s)^2} \sim 34$  nm),<sup>[62]</sup> further supporting the formation of elliptical micelles.

Interestingly, at  $t = 10.8$  s, the diffuse scattering starts to translate into two discrete symmetrical Bragg reflections centered at  $q_y = \pm 0.28 \text{ nm}^{-1}$ . These symmetric Bragg reflections sharpen and become more intense with time, reaching maximum scattering intensity at about  $t = 13.7$  s (Figure 2D,F). This suggests that the packing order of the BCP micelles is improved during the spin coating from  $t = 10.8$  s to  $t = 13.7$  s. The polymer volume fraction in the drying wet layer at this stage is about 0.1. For  $t \geq 13.7$  s, scattering along  $q_y$  starts to

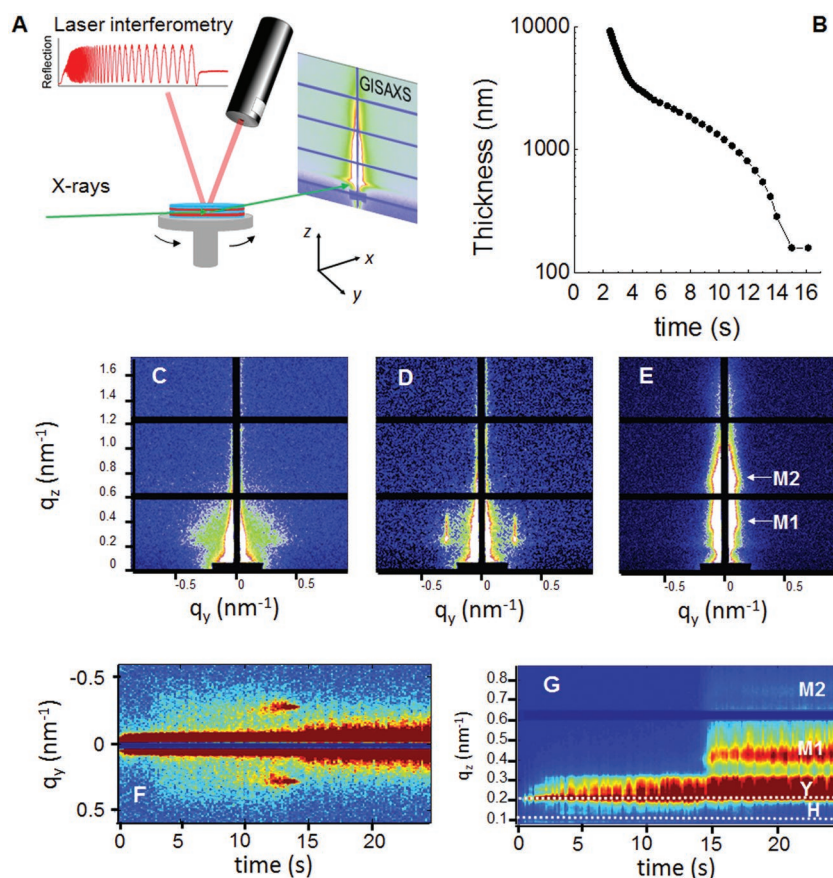


**Figure 2.** A) Schematic representation of the experimental setup used for in situ GISAXS/laser interferometry experiments during spin coating. The laser is incident along the  $y$ - $z$  plane at a  $45^\circ$  angle with respect to the  $x$ - $y$  plane on the spinning substrate. The specularly reflected laser signal is recorded using a photodiode. X-rays are incident along the  $x$ -direction at an angle of  $\alpha_i = 0.12^\circ$  and the sample-to-detector distance is 3200 mm. B) Evolution of the drying wet layer thickness retrieved from the laser interferometry data as a function of time during spin coating at 1000 rpm. C–E) Representative GISAXS patterns of the BCP thin film at 5, 13.4, and 19.5 s, respectively. F,G) Evolution of the horizontal,  $I(q_y)$ , and vertical,  $I(q_z)$ , time-lapse GISAXS intensity cuts taken at  $q_z = 0.27 \text{ nm}^{-1}$  and  $q_y = 0.05 \text{ nm}^{-1}$ , respectively. The most intense scattering peaks typical of the in-plane lamellar structure, M<sub>1</sub> and M<sub>2</sub>, are labeled in E,G). The broken horizontal lines in G) represent the position of the horizon (H) and Yoneda peak (Y).

vanish rapidly while DBSs concomitantly appear along the  $q_z$  direction (see Figure 2E,G).

In order to better understand the structural development of the BCP morphology during spin coating, **Figure 3** shows the most representative horizontal (at  $q_z = 0.27 \text{ nm}^{-1}$ ) and vertical (at  $q_y = 0.05 \text{ nm}^{-1}$ ) GISAXS intensity cuts at selected times while micellar assembly and structural transitions occur. The onset of the micellar structure organization is clearly visible on Figure 3A, with the appearance of a scattering peak along the horizontal  $q_y$  direction ( $I(q_y)$  cuts from 12.7 to 13.7 s). Such a peak is related to micellar packing in the drying wet film during solvent evaporation. Just before the micellar packing sets in (about 10 s), the BCP fraction calculated from the laser interferometry data is 0.1 (see Figure 2B). Solution SAXS analysis was performed at the same BCP concentration in PGMEA to assess the micellar shape (Figure S5, Supporting Information). Best fit of the 10 wt% BCP solution SAXS intensity indicates the development of core-shell rod-like polymeric micelles in

PGMEA, characterized by an almost dry PDMSB core of dimension  $R_{\text{core}}^{\text{PDMSB}} = 7 \text{ nm}$ , very close to the minor axis  $a$  of the ellipsoidal micelles observed at  $t = 5 \text{ s}$ . This suggests that over time the ellipsoidal micelles have grown along 1D to form cylindrical objects. Figure 3B,C evidence the packing of the PDMSB-*b*-PMMA core-shell cylindrical micelles into a hexagonal close-packed (HCP) array as shown by the two Bragg spots along the  $q_z$  direction, denoted as  $T_{10}$  and  $R_{10}$ , respectively. Interestingly, the appearance of these Bragg spots, above the Yoneda peak, clearly hints a parallel orientation of the  $\{10\}$  planes of the hexagonal rod-like micellar structure as regards to the substrate.<sup>[63]</sup> The intercylinder distance,  $a_{\text{CYL}}$ , was retrieved from the position of both the  $T_{10}$  and  $R_{10}$  Bragg spots, i.e.,  $a_i = 22 \text{ nm}$  (Figure 3C, Equation S2, Supporting Information and relative text).<sup>[30,63]</sup> The average size of the HCP domains as estimated from the peak width along  $q_y$  is 500 nm. The lack of higher order Bragg spots further suggests a short positional order of the hexagonal rod-like micellar structure. For  $t > 13.7 \text{ s}$ , the  $T_{10}$  and  $R_{10}$  Bragg spots suddenly vanish, and several intensity modulations along the vertical  $q_z$  direction appear (Figure 3D). These modulations next to the specular rod are associated with the formation of the parallel lamellar structure and the periodicity of this lamellar structure can be retrieved from the position of DBSs following Equation (1). Due to the overillumination of the sample and the scattering from the edges of the spinning substrate, a large background is present in the in situ data at the small  $q_y$  ( $q_y < 0.1 \text{ nm}^{-1}$  as seen in Figure 3A) and  $q_z$  ( $q_z < 0.4 \text{ nm}^{-1}$  as seen in Figure 3D) values. While the background along the  $q_y$  cuts does not overlap with the

signal from the sample, this background extends to the Yoneda and specular peaks along the  $q_z$  direction at  $q_y = 0.05 \text{ nm}^{-1}$ , causing a broadening of the signal. Consequently, we further decomposed the intensity along  $q_z$  by considering the sum of three Lorentzian peaks (M<sub>1</sub>, P<sub>1</sub>, and M<sub>2</sub>) plus a power law background in the range  $q_z > 0.3 \text{ nm}^{-1}$ , in order to accurately estimate the position of the lamellar peaks. Interestingly, an epitaxial relationship exists at the onset of the transformation of the hexagonal cylindrical micellar structure into the lamellar one since  $D_{10}^{\text{CYL}} = \sqrt{3}/2 a_{\text{CYL}} = D_{10}^{\text{LAM}} = 19 \text{ nm}$  at  $t = 13.7 \text{ s}$ . This observation clearly suggests that the final lamellar phase is nucleated from the hexagonally packed micellar structure, and the lamellae are formed through the merging of the cylinders along the  $\{10\}$  planes.<sup>[64–66]</sup>

The full structural formation and ordering mechanism of the PDMSB-*b*-PMMA copolymer during spin coating can thus be inferred by considering the simultaneous laser interferometry and the GISAXS results. **Figure 4** summarizes

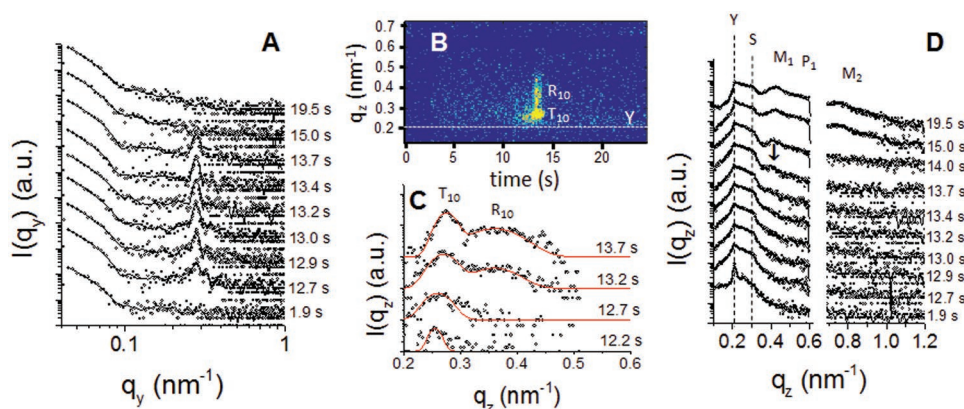


**Figure 3.** A) Selected GISAXS intensity cuts along the horizontal  $q_y$  direction taken at  $q_z = 0.27 \text{ nm}^{-1}$ . The black line is a curve obtained from the smoothing of the data by the Savitzky–Golay filter (polynomial order 2 and window length 5 points). B) Evolution of the vertical intensity cuts at  $q_y = 0.28 \text{ nm}^{-1}$ , i.e., along the (10) peak position for the cylindrical micellar assembly. The broken white line denotes the expected Yoneda peak position, Y.  $T_{10}$  and  $R_{10}$  are the Bragg spots for the parallel cylindrical structure. C) Selected intensity cuts along the vertical  $q_z$  direction at  $q_y = 0.28 \text{ nm}^{-1}$  (position of the diffraction peak). The red line is a fit using a constant background plus two Lorentzian peaks in order to retrieve the  $T_{10}$  and  $R_{10}$  reflections. D) Selected vertical intensity cuts along the vertical  $q_z$  direction at  $q_y = 0.05 \text{ nm}^{-1}$  (close to the specular rod). Y and S denote the Yoneda and specular peak positions, respectively, and  $M_1$ ,  $P_1$ ,  $M_2$ , and  $P_2$  denote the position of the *minus* and *plus* branch for the 1st and 2nd order DBSs. The black arrow points to the first appearance of the  $M_1$  branch at  $t = 13.7 \text{ s}$ . The black line is a curve obtained from the smoothing of the data by the Savitzky–Golay (polynomial order 2 and window length 5 points). The positions of the  $M_1$ ,  $P_1$ , and  $M_2$  reflections were retrieved by considering the sum of three Lorentzian peaks plus a power law background in the range  $q_z > 0.3 \text{ nm}^{-1}$ .

the evolution of the wet layer thickness, the solvent and BCP volume fractions and the integrated GISAXS intensities as a function of time during the spin coating. Five distinct stages can be differentiated. The first stage (I) is the lateral ejection of solution that leads to a fast decrease of the scattering intensity and is followed by the formation of a thick wet layer. In stage (II), THF first evaporates resulting in a wet layer thickness

change from 9 to about  $3 \mu\text{m}$  (from  $2.1 \text{ s} \leq t \leq 4 \text{ s}$ ). No structures are visible at this stage. After most of the THF has evaporated, the formation of core–shell elliptical micelles with a PDMSB core and a PMMA shell highly swollen by the selective PGMEA solvent takes place. The micellization process (micelle formation and 1D micellar growth) continues for the next 6–7 s as further solvent is evaporated from the drying wet

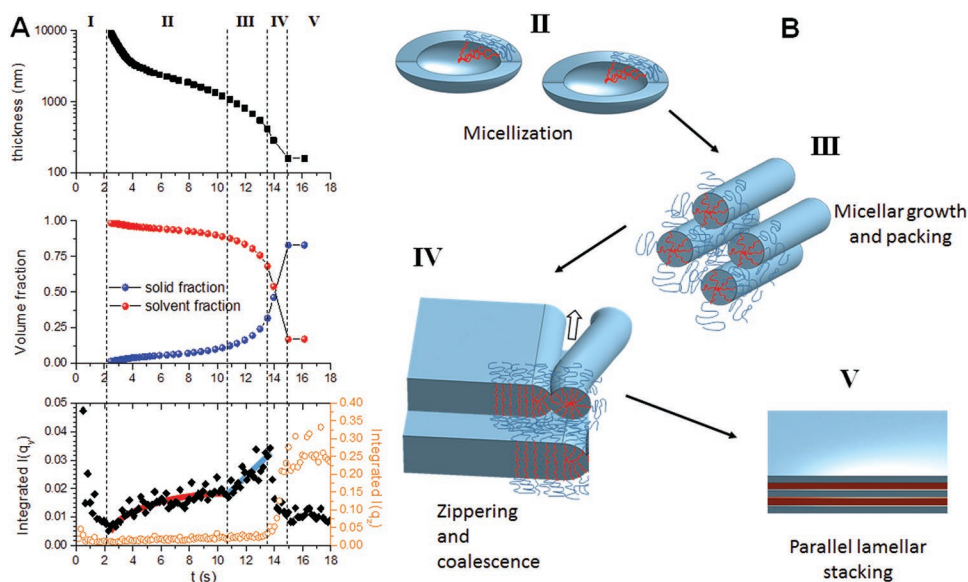


**Figure 4.** A) Time evolution of the thickness (top panel); solvent and solid volume fraction (middle panel); and integrated horizontal and vertical GISAXS intensities (bottom panel). The red and light blue curves are a guide for the eye to highlight the transition between stages (II) and (III). B) Proposed scheme for the processes occurring during spin coating. (II) After lateral solvent ejection (stage I), formation of ellipsoidal micelles with PDMSB core and PMMA shell occurs. (III) Micelles grow to form core–shell worm-like micelles oriented parallel to the substrate and aligned with the flow. The worm-like micelles tend to assemble forming large domains with a low degree of structural order. (IV) The core–shell worm-like micelles start to coalesce in the lateral direction *via* a zippering mechanism. (V) Lamellae parallel to the substrate are formed. A final BCP thin film thickness of 150 nm was measured at the end of the spin coating process.

layer. Suddenly, in stage (III), the intensity in the horizontal direction starts to rise steeply and diffraction signals appear on the GISAXS patterns (Figures 2D,F and 3A–C). At this stage, rod-like micelles made of a dry PDMSB core and a swollen PMMA shell start to pack in a HCP array with the cylindrical structures aligned parallel to the substrate. The intensity along  $q_y$  reaches its maximum value at about 13.7 s, before rapidly vanishing. Further fitting of the  $I(q_y)$  intensity cuts confirms that the first moderate intensity rise is due to the formation of dispersed BCP micelles, while the second steep intensity rise is related to the micellar packing (see Figure S6, Supporting Information). Moreover, the fitting results show the growth of the HCP domain size from an initial value of about 100 nm to a final value of 500 nm (Figure S6E, Supporting Information). In stage (IV), the decrease of the  $I(q_y)$  intensity is complemented by the increase of the  $I(q_z)$  intensity due to the formation of the parallel lamellar structure. The perfect match of the onset of the  $I(q_y)$  decrease and the  $I(q_z)$  increase, together with the epitaxial relationship between the two structures discussed above, suggests that the lamellar phase is generated from the transformation of the micellar cylindrical phase. The micellar cylindrical-to-lamellar phase transformation most probably involves lateral coalescence of adjacent cylinders through a zipper mechanism.<sup>[64,66]</sup> The driving force for this coalescence is related to the solvent evaporation from the PMMA shell, reducing the effective volume fraction of the PMMA phase with respect to the PDMSB one. This drives the system to a lower curvature structure (i.e., the lamellar phase in stage (IV)). Moreover, the coalescence between cylinders can also be facilitated by instabilities generated during the fast film drying, leading to cylinder bending in the direction parallel to the substrate due to the mechanical constraints induced by the drastic decrease of the wet layer thickness. These instabilities could resemble the Helfrich–Hurault instability mechanism described for polymeric columnar phases constrained in the vertical direction.<sup>[67]</sup> Finally, as most of the solvent is evaporated, further evolution of the BCP structure toward the thermodynamic equilibrium phase (i.e., the PMMA cylindrical phase observed on thermally annealed samples (see Figure S1, Supporting Information)) is hindered by the limited diffusion of the PDMSB-*b*-PMMA chains due to the approach of the PMMA glass transition in stage (V) leading to the quenching of the BCP morphology into the parallel lamellar structure. Interestingly, the micelles-to-lamellae transition appears feebly dependent of the deposition parameters (i.e., initial BCP concentration and spin coating rate) as the same multistage process was also retrieved for two different sets of initial deposition parameters as shown in Figure S7 in the Supporting Information (at 2250 rpm of a 2 wt% BCP solution in THF/PGMEA: 70/30, see Figure S7A,B, Supporting Information and at 1000 rpm of a 4 wt% BCP solution in THF/PGMEA: 70/30, see Figure S7C,D). Thus our conclusions are generally valid independently of the depositions parameters, unless the BCP composition and/or the solvent nature are modified. Indeed, we anticipate that the main parameter guiding the self-assembly process observed here during the BCP film deposition is the solvent selectivity, i.e., the ratio between THF and PGMEA. It should be noted that the BCP system considered herein allows additional reorganization steps with respect

to previously studied systems, such as PS-*b*-P2VP,<sup>[48]</sup> as the soft nature of the PDMSB block ( $T_g = -70$  °C) and selective solvent swelling of the PMMA phase provide high mobility to the PDMSB-*b*-PMMA chains, allowing for fast ordering and drastic morphological transitions until quite large solid contents. Alternatively, the system would vitrify in a micellar phase, probably during stage (III). Notably, the preferential 1D growth along the direction parallel to the substrate of the micelles appears to be the defining step inducing the parallel lamellar orientation. The mechanism observed here, is different with respect to the one reported by Ogawa et al. for PS-*b*-P2VP system spun cast from toluene, where fast solvent convection perpendicular to the substrate forces the system to adopt a vertical cylindrical morphology.<sup>[48]</sup>

In summary, block-copolymer ordering during spin coating is a complex phenomenon involving several crucial steps. Key in this multistep fast organization process is the PGMEA affinity for the PMMA phase combined to the rapid evaporation of the THF solvent. This selectivity triggers the formation of PDMSB core micellar structures “stable” in the drying wet layer. The micelles are able to further grow into rod-like core-shell micelles and assemble into a hexagonal columnar structure, characterized by a rather large correlation length (domain size  $\approx$  500 nm). The flexible PDMSB core nature ( $T_g = -70$  °C) and the swollen PMMA phase enables the subsequent rapid development of a highly ordered lamellar structure with uniform orientation as the solvent evaporates from the drying wet layer. This cylindrical-to-lamellar transition occurs through directional coalescence of the micelles in a very short time scale (about 1 s), much shorter than the previous micellar growth and assembly stages (about 10 s). This extended time window for the micellar growth and micellar assembly seems to be necessary to obtain highly ordered structures directly after spin coating. Reducing drastically the time available for the BCP micellar assembly could result in a more defective and randomly oriented lamellar phase with possibly smaller domains, as usually observed in as-cast BCP thin films. Our results suggest that the formation of such transient micellar phases, triggered by solvent selectivity, is a pivotal process that has to be controlled to obtain highly ordered structures directly after the deposition of BCP thin layers. The system under study is indeed able to form very large lamellar grains, with perfect parallel orientation without any further annealing step, in agreement with the direct STEM observation. Progress in the understanding of such a process and, more importantly, control of the key parameters to induce the desired BCP structure after solution-coating opens new opportunities for the fabrication of highly ordered nanotemplates derived from the self-assembly of BCP thin films. The judicious choice of (co)-solvent quality, evaporation rates or deposition parameters should allow a precise tailoring of the final BCP structure, even enabling the formation of highly ordered non-equilibrium phases, and further works along these lines are currently ongoing. Also, the use of in situ GISAXS combined with complementary techniques with a subsecond time resolution represents a powerful tool to study the effect of these parameters in real time, i.e., during solvent evaporation, and might serve as basis for future simulations and theoretical studies on BCP assembly dynamics.

## Supporting Information

Supporting Information is available from the Wiley Online Library or from the author.

## Acknowledgements

The ESRF and NWO are acknowledged for allocating beam time at the Dutch-Belgian beamline (DUBBLE) for the GISAXS experiments. A. Legrain and M. Zelsmann are acknowledged for STEM imaging. J. J. van Franeker is acknowledged for useful discussions around the laser interferometry. The authors acknowledge financial support from the Industrial Chair (Arkema/ANR) within the grant agreement no. AC-2013-365. This work was performed within the framework of the EquipEx ELORPrintTec ANR-10-EQPX-28-01 and the LabEx AMADEus ANR-10-LABEX-0042-AMADEUS with the help of the French state Initiative d'Excellence IdEx ANR-10-IDEX-003-02. G.P. acknowledges the Zernike Institute for Advanced Materials for the startup funds and the LabEx AMADEus visiting professor grant received from the University of Bordeaux.

## Conflict of Interest

The authors declare no conflict of interest.

## Keywords

block copolymers, in situ GISAXS, micelles, ordering, selective solvent, spin coating

Received: September 24, 2018  
Revised: December 10, 2018  
Published online: January 18, 2019

- [1] M. J. Fasolka, A. M. Mayes, *Annu. Rev. Mater. Res.* **2001**, *31*, 323.  
[2] M. Lazzari, M. A. López-Quintela, *Adv. Mater.* **2003**, *15*, 1583.  
[3] I. W. Hamley, *Prog. Polym. Sci.* **2009**, *34*, 1161.  
[4] T. Thurn-Albrecht, J. Schotter, G. A. Kastle, N. Emley, T. Shibauchi, L. Krusin-Elbaum, K. Guarini, C. T. Black, M. T. Tuominen, T. P. Russell, *Science* **2000**, *290*, 2126.  
[5] A. Ethirajan, U. Wiedwald, H.-G. Boyen, B. Kern, L. Han, A. Klimmer, F. Weigl, G. Kästle, P. Ziemann, K. Fauth, J. Cai, R. J. Behm, A. Romanyuk, P. Oelhafen, P. Walther, J. Biskupek, U. Kaiser, *Adv. Mater.* **2007**, *19*, 406.  
[6] S. O. Kim, H. H. Solak, M. P. Stoykovich, N. J. Ferrier, J. J. De Pablo, P. F. Nealey, *Nature* **2003**, *424*, 411.  
[7] R. A. Segalman, *Mater. Sci. Eng., R* **2005**, *48*, 191.  
[8] T. Hashimoto, K. Tsutsumi, Y. Funaki, *Langmuir* **1997**, *13*, 6869.  
[9] E. A. Jackson, M. A. Hillmyer, *ACS Nano* **2010**, *4*, 3548.  
[10] M. M. Pendergast, R. Mika Dorin, W. A. Phillip, U. Wiesner, E. M. V. Hoek, *J. Membr. Sci.* **2013**, *444*, 461.  
[11] Y. S. Jung, W. Jung, H. L. Tuller, C. A. Ross, *Nano Lett.* **2008**, *8*, 3776.  
[12] X. Wang, K. Ehrhardt, C. Tallet, M. Warengem, A. Baron, A. Aradian, M. Kildemo, V. Ponsinet, *Opt. Laser Technol.* **2017**, *88*, 85.  
[13] P. Mokarian-Tabari, R. Senthamaraiannan, C. Glynn, T. W. Collins, C. Cummins, D. Nugent, C. O'Dwyer, M. A. Morris, *Nano Lett.* **2017**, *17*, 2973.  
[14] H. S. Lim, J. H. Lee, J. J. Walsh, E. L. Thomas, *ACS Nano* **2012**, *6*, 8933.  
[15] E. J. W. Crossland, M. Kamperman, M. Nedelcu, C. Ducati, U. Wiesner, D.-M. Smilgies, G. E. S. Toombes, M. A. Hillmyer, S. Ludwigs, U. Steiner, H. J. Snaith, *Nano Lett.* **2009**, *9*, 2807.  
[16] C. Guo, Y.-H. Lin, M. D. Witman, K. A. Smith, C. Wang, A. Hexemer, J. Strzalka, E. D. Gomez, R. Verduzco, *Nano Lett.* **2013**, *13*, 2957.  
[17] B. Smarsly, D. Grosso, T. Brezesinski, N. Pinna, C. Boissière, M. Antonietti, C. Sanchez, *Chem. Mater.* **2004**, *16*, 2948.  
[18] B. de Boer, U. Stalmach, H. Nijland, G. Hadziioannou, *Adv. Mater.* **2000**, *12*, 1581.  
[19] S. H. Kim, M. J. Misner, T. Xu, M. Kimura, T. P. Russell, *Adv. Mater.* **2004**, *16*, 226.  
[20] C. Tang, A. Tracz, M. Kruk, R. Zhang, D.-M. Smilgies, K. Matyjaszewski, T. Kowalewski, *J. Am. Chem. Soc.* **2005**, *127*, 6918.  
[21] K. A. Cavicchi, K. J. Berthiaume, T. P. Russell, *Polymer* **2005**, *46*, 11635.  
[22] S. Ham, C. Shin, E. Kim, D. Y. Ryu, U. Jeong, T. P. Russell, C. J. Hawker, *Macromolecules* **2008**, *41*, 6431.  
[23] W. A. Phillip, M. A. Hillmyer, E. L. Cussler, *Macromolecules* **2010**, *43*, 7763.  
[24] J. W. Jeong, W. I. Park, M. Kim, C. A. Ross, Y. S. Jung, *Nano Lett.* **2011**, *11*, 4095.  
[25] S. Park, X. Cheng, A. Böker, L. Tsarkova, *Adv. Mater.* **2016**, *28*, 6900.  
[26] C. Sinturel, M. Vayer, M. Morris, M. A. Hillmyer, *Macromolecules* **2013**, *46*, 5399.  
[27] P. W. Majewski, K. G. Yager, *J. Phys.: Condens. Matter* **2016**, *28*, 403002.  
[28] P. Müller-Buschbaum, *Eur. Polym. J.* **2016**, *81*, 470.  
[29] X. Gu, I. Gunkel, A. Hexemer, W. Gu, T. P. Russell, *Adv. Mater.* **2014**, *26*, 273.  
[30] S. Samant, J. Strzalka, K. G. Yager, K. Kisslinger, D. Grolman, M. Basutkar, N. Salunke, G. Singh, B. Berry, A. Karim, *Macromolecules* **2016**, *49*, 8633.  
[31] P. W. Majewski, K. G. Yager, *Soft Matter* **2016**, *12*, 281.  
[32] D. Posselt, J. Zhang, D.-M. Smilgies, A. V. Berezkin, I. I. Potemkin, C. M. Papadakis, *Prog. Polym. Sci.* **2017**, *66*, 80.  
[33] A. Knoll, A. Horvat, K. S. Lyakhova, G. Krausch, G. J. A. Sevink, A. V. Zvelindovsky, R. Magerle, *Phys. Rev. Lett.* **2002**, *89*, 035501.  
[34] G. E. Stein, E. J. Kramer, X. Li, J. Wang, *Macromolecules* **2007**, *40*, 2453.  
[35] A. Modi, A. Karim, M. Tsige, *Macromolecules* **2018**, *51*, 7186.  
[36] S. Y. Heriot, R. A. L. Jones, *Nat. Mater.* **2005**, *4*, 782.  
[37] S. Ebbens, R. Hodgkinson, A. J. Parnell, A. Dunbar, S. J. Martin, P. D. Topham, N. Clarke, J. R. Howse, *ACS Nano* **2011**, *5*, 5124.  
[38] D. T. W. Toolan, E. ul Haq, A. Dunbar, S. Ebbens, N. Clarke, P. D. Topham, J. R. Howse, *J. Polym. Sci., Part B: Polym. Phys.* **2013**, *51*, 875.  
[39] G. Portale, D. Cavallo, G. C. Alfonso, D. Hermida-Merino, M. Van Drongelen, L. Balzano, G. W. M. Peters, J. G. P. Goossens, W. Bras, *J. Appl. Crystallogr.* **2013**, *46*, 1681.  
[40] G. Portale, D. Hermida-Merino, W. Bras, *Eur. Polym. J.* **2016**, *81*, 415.  
[41] K. W. Chou, B. Yan, R. Li, E. Q. Li, K. Zhao, D. H. Anjum, S. Alvarez, R. Gassaway, A. Biocca, S. T. Thoroddsen, A. Hexemer, A. Amassian, *Adv. Mater.* **2013**, *25*, 1923.  
[42] J. J. van Franeker, D. Hermida-Merino, C. Gommès, K. Arapov, J. J. Michels, R. A. J. Janssen, G. Portale, *Adv. Funct. Mater.* **2017**, *27*, 1702516.  
[43] S. Pröller, F. Liu, C. Zhu, C. Wang, T. P. Russell, A. Hexemer, P. Müller-Buschbaum, E. M. Herzig, *Adv. Energy Mater.* **2016**, *6*, 1501580.  
[44] S. Yu, G. Santoro, K. Sarkar, B. Dicke, P. Wessels, S. Bommel, R. Döhrmann, J. Perlich, M. Kuhlmann, E. Metwalli, J. F. H. Risch, M. Schwartzkopf, M. Drescher, P. Müller-Buschbaum, S. V. Roth, *J. Phys. Chem. Lett.* **2013**, *4*, 3170.

- [45] X. Gu, J. Reinspach, B. J. Worfolk, Y. Diao, Y. Zhou, H. Yan, K. Gu, S. Mannsfeld, M. F. Toney, Z. Bao, *ACS Appl. Mater. Interfaces* **2016**, *8*, 1687.
- [46] F. Liu, Y. Gu, C. Wang, W. Zhao, D. Chen, A. L. Briseno, T. P. Russell, *Adv. Mater.* **2012**, *24*, 3947.
- [47] H. Ogawa, T. Miyazaki, K. Shimokita, A. Fujiwara, M. Takenaka, T. Yamada, Y. Sugihara, M. Takata, *J. Appl. Crystallogr.* **2013**, *46*, 1610.
- [48] H. Ogawa, M. Takenaka, T. Miyazaki, A. Fujiwara, B. Lee, K. Shimokita, E. Nishibori, M. Takata, *Macromolecules* **2016**, *49*, 3471.
- [49] K. Aissou, M. Mumtaz, G. Fleury, G. Portale, C. Navarro, E. Cloutet, C. Brochon, C. A. Ross, G. Hadziioannou, *Adv. Mater.* **2015**, *27*, 261.
- [50] Y. Rho, K. Aissou, M. Mumtaz, W. Kwon, G. Pécastaings, C. Mocuta, S. Stanescu, E. Cloutet, C. Brochon, G. Fleury, G. Hadziioannou, *Small* **2015**, *11*, 6377.
- [51] P. Busch, M. Rauscher, D.-M. M. Smilgies, D. Posselt, C. M. Papadakis, *J. Appl. Crystallogr.* **2006**, *39*, 433.
- [52] A. Sepe, J. Zhang, J. Perlich, D.-M. Smilgies, D. Posselt, C. M. Papadakis, *Eur. Polym. J.* **2016**, *81*, 607.
- [53] J. Zhang, D. Posselt, D.-M. Smilgies, J. Perlich, K. Kyriakos, S. Jaksch, C. M. Papadakis, *Macromolecules* **2014**, *47*, 5711.
- [54] Z. Di, D. Posselt, D.-M. Smilgies, C. M. Papadakis, *Macromolecules* **2010**, *43*, 418.
- [55] Z. Di, D. Posselt, D.-M. Smilgies, R. Li, M. Rauscher, I. I. Potemkin, C. M. Papadakis, *Macromolecules* **2012**, *45*, 5185.
- [56] M. A. Chavis, D.-M. Smilgies, U. B. Wiesner, C. K. Ober, *Adv. Funct. Mater.* **2015**, *25*, 3057.
- [57] W. Bai, K. G. Yager, C. A. Ross, *Macromolecules* **2015**, *48*, 8574.
- [58] H. Cho, H. Park, T. P. Russell, S. Park, *J. Mater. Chem.* **2010**, *20*, 5047.
- [59] J. P. Spatz, S. Mössmer, C. Hartmann, M. Möller, T. Herzog, M. Krieger, H. G. Boyen, P. Ziemann, B. Kabius, *Langmuir* **2000**, *16*, 407.
- [60] C. S. Thomas, L. Xu, B. D. Olsen, *Biomacromolecules* **2012**, *13*, 2781.
- [61] J. C. Brendel, F. Liu, A. S. Lang, T. P. Russell, M. Thelakkat, *ACS Nano* **2013**, *7*, 6069.
- [62] W. Van de Sande, A. Persoons, *J. Phys. Chem.* **1985**, *89*, 404.
- [63] B. Lee, I. Park, J. Yoon, S. Park, J. Kim, K.-W. Kim, T. Chang, M. Ree, *Macromolecules* **2005**, *38*, 4311.
- [64] S. Sakurai, T. Momii, K. Taie, M. Shibayama, S. Nomura, T. Hashimoto, *Macromolecules* **1993**, *26*, 485.
- [65] T.-Y. Lo, R.-M. Ho, P. Georgopoulos, A. Avgeropoulos, T. Hashimoto, *ACS Macro Lett.* **2013**, *2*, 190.
- [66] Y. Liu, M. Li, R. Bansil, M. Steinhart, *Macromolecules* **2007**, *40*, 9482.
- [67] G. G. Pereira, *J. Chem. Phys.* **2002**, *117*, 1878.